

Generation-dependent charge carrier transport in Cu(In,Ga)Se₂/CdS/ZnO thin-film solar-cells

Melanie Nichterwitz,^{1,a)} Raquel Caballero,^{1,2} Christian A. Kaufmann,¹ Hans-Werner Schock,¹ and Thomas Unold¹

¹*Helmholtz-Zentrum Berlin für Materialien und Energie, Hahn-Meitner-Platz 1, D-14109 Berlin, Germany*

²*Universidad Autónoma de Madrid, Departamento de Física Aplicada, C/ Francisco Tomás y Valiente 7, 28049 Madrid, Spain.*

(Received 6 November 2012; accepted 7 January 2013; published online 29 January 2013)

Cross section electron-beam induced current (EBIC) and illumination-dependent current voltage (IV) measurements show that charge carrier transport in Cu(In,Ga)Se₂ (CIGSe)/CdS/ZnO solar-cells is generation-dependent. We perform a detailed analysis of CIGSe solar cells with different CdS layer thicknesses and varying Ga-content in the absorber layer. In conjunction with numerical simulations, EBIC and IV data are used to develop a consistent model for charge and defect distributions with a focus on the heterojunction region. The best model to explain our experimental data is based on a p+ layer at the CIGSe/CdS interface leading to generation-dependent transport in EBIC at room temperature. Acceptor-type defect states at the CdS/ZnO interface cause a significant reduction of the photocurrent in the red-light illuminated IV characteristics at low temperatures (red kink effect). Shallow donor-type defect states at the p+ layer/CdS interface of some grains of the absorber layer are responsible for grain specific, i.e., spatially inhomogeneous, charge carrier transport observed in EBIC. © 2013 American Institute of Physics. [<http://dx.doi.org/10.1063/1.4788827>]

I. INTRODUCTION

Cu(In,Ga)Se₂ (CIGSe)/CdS/ZnO solar-cells consist of a multilayer stack of semiconductor and metallic layers. Due to the complexity of the structure with two heterojunctions (CIGSe/CdS and CdS/ZnO) involved, there are still some open questions concerning defect and charge distributions and the influences on charge carrier transport.

One important finding reported in the literature is the occurrence of generation-dependent charge carrier transport in electron-beam induced current (EBIC) measurements on cross sections of CIGSe solar cells¹ and illumination-dependent current voltage (IV) analysis.^{2–4} In EBIC, a significant decrease of the short circuit current was observed for electron beam irradiation in the absorber bulk without generation in the heterojunction region.¹ In IV analysis, the solar cell current was found to decrease significantly under forward bias, which leads to the typical “kink” shape of the IV curve.^{2–4} The phenomenon is denoted as “red kink” if it only occurs under red light illumination. Several models have been proposed, which are all based on the assumption of a high density of acceptor-type defect states. These are either located in the absorber layer close to the CIGSe/CdS interface (p+ layer),^{1,4,5} within the CdS layer^{2,3,6} or at the CdS/ZnO interface.^{7,8} In all models, the defect states are mostly occupied by electrons for generation conditions that imply a low hole density in the heterojunction region (red light illumination, electron beam irradiation in the bulk of the absorber layer). The resulting high local negative charge density leads to a significant current decrease for short circuit conditions in EBIC and in the forward bias range in IV analysis. In the following, the models are explained in more detail.

A. p+ layer

The local doping density of the CIGSe layer close to the interface to CdS in a completed solar cell has not been clarified yet. Some publications suggest n-type conductivity either caused by Cd diffusion^{9,10} or the formation of an n-type defect compound with an enlarged bandgap energy.¹¹ Other publications suggest a p+ layer (high density of acceptor-type defect states)⁵ or a p+ layer and additional donor-type defect states at the p+ layer/CdS interface.¹² It was shown that a p+ layer can account for a kink for red and white light illumination.^{4,13} Kniese *et al.* presented numerical simulations demonstrating that a p+ layer and additional donor-type defect states at the p+ layer/CdS interface can also account for generation-dependent transport in EBIC.¹ As possible microscopic origins for a p+ layer, the acceptor configurations of the amphoteric ($V_{Se} - V_{Cu}$) and ($In_{Cu} + 2V_{Cu}$) (DX center) defect complexes as calculated by Lany and Zunger^{14,15} were suggested.^{16,17} An alternative explanation is based on field induced Cu-migration in CIGSe.^{18,19} Cu-ions drift away from the heterointerface until an equilibrium is reached. This leads to a Cu-depleted CIGSe surface with a higher acceptor density than the bulk of the material.

B. Deep acceptors in the CdS layer

An alternative explanation for the red kink effect in IV is based on deep acceptor-type defect states in the CdS in addition to shallow n-type doping.^{2,3} The degree of compensation, i.e., the effective charge density in the CdS, depends on the occupation of this deep acceptor. For illumination with light which is not absorbed in the CdS (red light), the local hole density is low and the acceptor is mainly occupied by electrons. The positive charge of the

^{a)}Electronic mail: melanie.nichterwitz@helmholtz-berlin.de.

shallow n-type doping is either reduced or even overcompensated, and most of the potential drops across the CdS layer. For white light illumination, photo-generated holes are trapped in the CdS, and more potential drops across the CIGSe layer. Hou *et al.*² concluded that for red light illumination, collection in the absorber layer is limited to diffusion instead of drift. This can reduce the photocurrent especially under forward bias thereby leading to a red kink. In the model by Eisgruber *et al.*,³ a spike in the conduction band at the CIGSe/CdS interface serves as an effective barrier for the electron current from CIGSe into CdS for red light illumination at low temperatures. For white light illumination, the electron density at the interface is higher due to the generation in the CdS layer. Consequently, the effective barrier is lower and the current is not impeded.

C. Acceptors at the buffer/window interface

Numerical simulations showed that acceptor-type defect states at the buffer/window interface can also cause a kink in the IV curve.⁷ Nguyen *et al.*²⁰ found that such interface states do play a role, in particular, in solar cells with In(OH,S) buffer layers. In devices with CdS, the defect density seemed to be rather low ($7 \times 10^9 \text{ cm}^{-2}$). Another possible configuration leading to a red kink is given by a high density of interface defects at both front heterointerfaces (CIGSe/CdS and CdS/ZnO interfaces).⁸ If the Fermi level is pinned by donor-type defect states at the CIGSe/CdS interface close to the conduction band minimum and further away at the CdS/ZnO interface by acceptor-type defect states, there is field inversion in the CdS. This can form a barrier for the electron current from the absorber layer.⁸

So far, a quantitative description and numerical simulations of generation-dependent charge carrier transport were only presented for either one of the experimental effects in IV and EBIC (mostly IV). In the present work, we will derive a consistent model for EBIC and IV data of the same solar cell. The advantage of this combination of techniques is to obtain both spatially resolved and integral information about charge carrier transport for different generation conditions. We performed cross section EBIC and IV measurements on CIGSe/CdS/ZnO solar cells with absorber layers of varying Ga-content and different CdS layer thicknesses. With one dimensional numerical simulations, we test the existing models and develop a consistent model for space charge distributions, interface properties, and resulting transport properties.

The present publication is organized as follows. Experimental details and the basics of EBIC and the numerical simulations are given in Sec. II. In Sec. III, the results of EBIC and IV measurements on CuInSe₂ (CISe) solar cells, a series of CuInSe₂ solar cells with varying CdS thickness, and a series of CIGSe solar cells with absorber layers with varying Ga-content and corresponding numerical simulations are presented. After that, we summarize our results and discuss them further in the frame of conclusions drawn in the literature in Sec. IV. In Sec. V, our conclusions are summarized briefly.

II. EXPERIMENTAL DETAILS AND METHODS

A. Experimental details

The solar cells used for the present study were fabricated at the Helmholtz-Zentrum Berlin and use soda lime glass as a substrate. They consist of a multilayer stack of a sputtered molybdenum back contact ($\approx 1 \mu\text{m}$), an evaporated p-type CIGSe absorber layer ($\approx 2 \mu\text{m}$), an n-type CdS buffer layer ($\approx 50 \text{ nm}$) deposited in a chemical bath, and a sputtered double layer of intrinsic ZnO (i-ZnO) and Al-doped ZnO (Al:ZnO) (n-type). On top of the ZnO window layer, there is an evaporated Ni:Al contact grid.

The CIGSe absorber layers were evaporated in a multi-stage coevaporation process²¹ based on the three-stage physical vapor deposition process.²² During the first stage, a layered precursor of In, Ga, and Se is deposited at a substrate temperature of 330°C . The evaporation of In and Se and that of Ga and Se is carried out separately in order to control the final Ga to In ratio ($[\text{Ga}]/([\text{Ga}] + [\text{In}]) =: \text{Ga/III}$) of the CIGSe layer. During the second stage, Cu and Se are evaporated at a substrate temperature of 525°C . The stoichiometric point of CIGSe is detected by means of laser light scattering.²³ In a *standard* process, Cu and Se are evaporated until the layer has a Cu-content $[\text{Cu}]/([\text{Ga}] + [\text{In}]) =: \text{Cu/III}$ of approximately 1.15. During stage three, In, Ga, and Se are evaporated simultaneously until the layer has a final Cu-content of $\text{Cu/III} = 0.7\text{--}0.9$.

For EBIC, the electron-beam induced current I_{EBIC} is transformed into a voltage, amplified by use of a transimpedance amplifier and eight bit digitized. The measurements were performed in a Zeiss Leo Gemini 1530 microscope with a field emission gun using electron beam currents from 7 to 315 pA and electron beam energies from 5 to 18 keV . For current to voltage conversion and amplification, a Femto DLPCA 200 transimpedance amplifier was used.

The IV measurements were performed in a closed-cycle helium cryostat by use of a Keithley 238 source measure unit. The sample temperature was determined by a calibrated Si-diode mounted on a glass substrate identical to the solar cell substrates. For illumination, a HMI (helium medium arc length iodide) lamp of type Osram HMI 575 W/SEL was used. The light denoted as red light in the following consists of the long wavelength range of the lamp spectrum with a cut-off wavelength at 630 nm . The absorption edge of CdS with a bandgap energy of approximately 2.4 eV corresponds to a wavelength of 517 nm , which means that red light is not absorbed in the CdS via band-to-band transitions. Before the measurement, the solar cells were stored in the dark for at least 1 h at a temperature of 320 K for relaxation.

B. Electron-beam induced current

In an EBIC experiment, the electron beam of a scanning electron microscope is used to generate electron-hole pairs in the semiconductor layers of a solar cell. These can either recombine or they are collected, i.e., measurable as an external current, which depends on the position of irradiation, the electron beam current I_b and energy E_b and the electronic properties of the solar cell. For the present study, we used

the cross section configuration, which is depicted in Figure 1. A line profile of short-circuit current values I_{EBIC} perpendicular to the pn-junction (direction x) will be called EBIC profile in this work.

For a simple and instructive analytical description of EBIC data, translation invariance parallel to the pn-junction is assumed and the problem is restricted to one dimensional expressions. The probability that a charge carrier generated at position x is collected, is given by the collection function $f_c(x)$. It can be obtained from the following differential equation for the field free region of a p-type semiconductor under low injection conditions:²⁴

$$D_e \Delta f_c(x) - \frac{f_c(x)}{\tau_e} = 0, \quad (1)$$

where D_e stands for the electron diffusion coefficient and τ_e for the electron lifetime. With the boundary conditions $f_c(x_{\text{SCR}}) = 1$ and $-D_e \frac{d}{dx} f_c(x_C) = S_C f_c(x_C)$, a solution for $f_c(x)$ is given by

$$f_c(x) = \frac{\frac{1}{L_e} \cosh\left(\frac{x - x_C}{L_e}\right) - \frac{S_C}{D_e} \sinh\left(\frac{x - x_C}{L_e}\right)}{\frac{S_C}{D_e} \sinh\left(\frac{x_C - x_{\text{SCR}}}{L_e}\right) + \frac{1}{L_e} \cosh\left(\frac{x_C - x_{\text{SCR}}}{L_e}\right)}, \quad (2)$$

where x_{SCR} stand for the position of the edge of the space charge region, x_C for the position of a semiconductor-metal contact, S_C for the contact recombination velocity of electrons, and $L_e = \sqrt{D_e \tau_e}$ for the electron (minority charge carrier) diffusion length.

I_{EBIC} can be expressed as a convolution of the collection function $f_c(x)$ and the lateral generation function of the electron beam $g(x)$ ²⁴

$$I_{\text{EBIC}}(a) = \int_0^{\infty} g(x, a) f_c(x) dx, \quad (3)$$

where a denotes the position of irradiation.

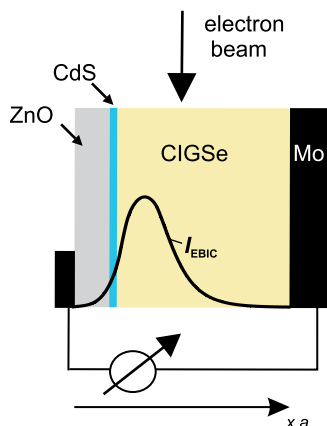


FIG. 1. Schematic of an EBIC experiment on a CIGSe/CdS/ZnO solar cell.

C. Numerical simulations

The numerical simulations of EBIC and IV data shown in this publication were performed by use of the one-dimensional device simulator SCAPS.²⁵ The simulation algorithm finds numerical solutions to the Poisson equation and the continuity equations for electrons and holes. For the transport mechanism across the heterojunctions, thermionic field emission is assumed, i.e., intraband tunneling is included. For charge carrier generation in EBIC, an electron beam generation profile according to the equations given in Ref. 26 was used. The basic set of parameters for a CIGSe solar cell (denoted as standard) is listed in Table I and changes to these parameters are given in the text or figure captions. If not stated differently, the capture cross sections of electrons and holes are assumed to be $\sigma_e = 10^{-15} \text{ cm}^2$ and $\sigma_h = 10^{-13} \text{ cm}^2$ for acceptors, and $\sigma_e = 10^{-13} \text{ cm}^2$ and $\sigma_h = 10^{-15} \text{ cm}^2$ for donors and flatband alignment of the conduction band is assumed. The electronic band diagram for the standard set of parameters is depicted in Figure 2.

TABLE I. SCAPS simulation parameters of the standard CIGSe solar cell: $S_{e,h}$: recombination velocity of electrons and holes, Φ_b : contact barrier, d : thickness, E_g : bandgap energy, χ_e : electron affinity, ϵ : dielectric permittivity, $\mu_{e,h}$: electron and hole mobility, $v_{th,e,h}$: thermal velocity of electrons and holes, $N_{C,V}$: effective density of states in conduction and valence band, N_d shallow n-type doping density, N_a shallow p-type doping density, N_t defect density, E_t defect energy (monoenergetic), $\sigma_{e,h}$: capture cross section for electrons and holes, $\tau_{e,h}$: lifetime of electrons and holes, $L_{e,h}$: diffusion length of electrons and holes.

| | Contacts | | | |
|-------------------------------------|-------------------------|----------------------|----------------------|----------------------|
| | Front | Back | | |
| S_e (cm/s) | 1×10^7 | 1×10^7 | | |
| S_h (cm/s) | 1×10^7 | 1×10^7 | | |
| Φ_b (eV) | 0 | 0 | | |
| | Layers | | | |
| | ZnO | i-ZnO | CdS | CIGSe |
| d (μm) | 0.37 | 0.08 | 0.05 | 1.7 |
| E_g (eV) | 3.3 | 3.3 | 2.4 | 1.0 |
| χ_e (eV) | 4.5 | 4.5 | 4.5 | 4.5 |
| ϵ | 9 | 9 | 10 | 13.6 |
| μ_e (cm^2/Vs) | 40 | 40 | 40 | 40 |
| μ_h (cm^2/Vs) | 10 | 10 | 10 | 10 |
| $v_{th,e}$ (cm/s) | 1×10^7 | 1×10^7 | 1×10^7 | 1×10^7 |
| $v_{th,h}$ (cm/s) | 1×10^7 | 1×10^7 | 1×10^7 | 1×10^7 |
| N_C (cm^{-3}) | 2.2×10^{18} | 2.2×10^{18} | 2.2×10^{18} | 2.2×10^{18} |
| N_V (cm^{-3}) | 1.8×10^{19} | 1.8×10^{19} | 1.8×10^{19} | 1.8×10^{19} |
| N_d (cm^{-3}) | 1×10^{18} | 1×10^{17} | 1×10^{16} | |
| N_a (cm^{-3}) | | | | 2×10^{15} |
| | Defects (acceptor type) | | | |
| | | | | |
| N_t (cm^{-3}) | 1×10^{16} | 1×10^{16} | 1×10^{15} | 2×10^{15} |
| E_t (eV) | 1.65 | 1.65 | 1.2 | 0.5 |
| σ_e (cm^2) | 1×10^{-15} | 1×10^{-15} | 1×10^{-15} | 2×10^{-14} |
| σ_h (cm^2) | 1×10^{-13} | 1×10^{-13} | 1×10^{-12} | 1×10^{-13} |
| | Calculated quantities | | | |
| | | | | |
| τ_e (ns) | 10 | 10 | 100 | 2.5 |
| τ_h (ns) | 0.1 | 0.1 | 0.1 | 0.5 |
| L_e (μm) | 1 | 1 | 3.2 | 0.51 |
| L_h (μm) | 0.051 | 0.051 | 0.029 | 0.11 |

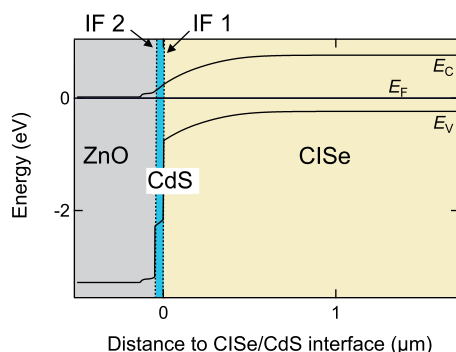


FIG. 2. Simulated electronic band diagram of a CIGSe solar cell for the simulation parameters listed in Table I ($T = 300$ K).

III. RESULTS

In this section, we present experimental results of EBIC and IV measurements and corresponding numerical simulations of CIGSe solar cells (Subsections III B and III C), a series of CIGSe solar cells with varying CdS layer thickness (Subsection III D), and a series of CIGSe solar cells with absorber layers of varying Ga-content (Subsection III E).

A. Room temperature IV data

Table II shows the room-temperature solar cell parameters and absorber layer compositions of the solar cells used for the present study. Two different series of solar cells were investigated: a varying Ga-content of the absorber layer (Ga-series) and different CdS layer thicknesses (CdS-series). Please note that our results and conclusions may only be representative for a large part of the solar cells from our lab with absorber layers deposited in a multistage evaporation process. Different deposition processes and process parameters can lead to devices with substantially different electrical properties.

B. EBIC

We used CIGSe solar cells, because their electronic properties are easier to describe than those of CIGSe solar cells,

TABLE II. Solar cell parameters and absorber layer compositions of the solar cells with absorber layers of varying Ga-content (Ga-series) and different CdS layer thicknesses (CdS-series). The average values of all solar cells of the same substrate are given (solar cells with a deviation of more than 20% in efficiency from the maximum value were excluded).

| | V_{oc} (mV) | j_{sc} (mA/cm ²) | FF (%) | η (%) | Cu/III | Ga/III |
|------------------|------------------|-----------------------------------|-----------|---------------|--------|--------|
| Ga-series | | | | | | |
| Ga/III = | | | | | | |
| 0 (CIGSe) | 460 | 40.5 | 71.7 | 13.4 | 0.83 | 0 |
| 0.3 | 655 | 30.6 | 72.8 | 14.6 | 0.77 | 0.34 |
| 0.5 | 657 | 27.8 | 69.8 | 12.7 | 0.76 | 0.50 |
| 0.7 | 762 | 21.9 | 60.0 | 10.0 | 0.85 | 0.73 |
| 1 | 696 | 12.4 | 47.3 | 4.1 | 0.89 | 1 |
| CdS-series | | | | | | |
| d_{CdS} (nm) = | | | | | | |
| 25 | 421 | 41.1 | 67.0 | 11.6 | 0.72 | 0 |
| 50 | 442 | 38.1 | 70.8 | 11.9 | 0.72 | 0 |
| 120 | 414 | 37.8 | 61.4 | 9.6 | 0.72 | 0 |
| 170 | 331 | 35.2 | 54.6 | 6.4 | 0.72 | 0 |

which often exhibit a gradient in Ga-content throughout the absorber layer. In comparative studies, we found, however, that our results are transferable to CIGSe solar cells with absorber layers of low Ga-content (≤ 0.35) and a similar Cu-content.²⁷

In Figure 3, a secondary electron (SE) image (a) and corresponding EBIC maps (b) recorded with different electron beam energies of a fractured CIGSe solar-cell cross section are shown. From these EBIC maps, line profiles perpendicular to the pn-junction were extracted, which are shown in Figure 4(a).

In Figure 4(b), EBIC profiles calculated according to Eq. (3) are displayed. f_c is assumed to be 1 in the space charge region because of field-assisted charge carrier collection. In the field free region, Eq. (2) is valid. The parameters are adjusted such that the measured and calculated profiles for an electron beam energy of 18 keV coincide. Measured and calculated profiles deviate significantly and a simulation of the measured curves for different electron beam energies is not possible with a constant set of parameters, i.e., a fixed collection function. At a certain distance from the CIGSe/CdS interface, which depends on the electron beam energy, the measured current starts to decrease significantly. The dependence of the width of the profile maxima on electron beam energy is more pronounced than expected. The abrupt and E_b -dependent current decrease has also been observed by Kniese *et al.*¹ and will be denoted as EBIC kink in the following. Since the extension of the generation volume is larger for a higher electron beam energy, this finding shows that charge carrier transport is generation-dependent: there is a significant current decrease for irradiation without generation in the heterojunction region.

In the following, we will show numerical simulations of EBIC profiles for simulation parameters according to the models for generation-dependent charge carrier transport discussed in the literature. These are: a p+ layer at the CIGSe/CdS interface (IF1), a high density of deep acceptor-type defect states in the CdS layer, and a high density of acceptor-type defect states at the CdS/ZnO interface (IF2). The parameters for these simulations are summarized in Table III.

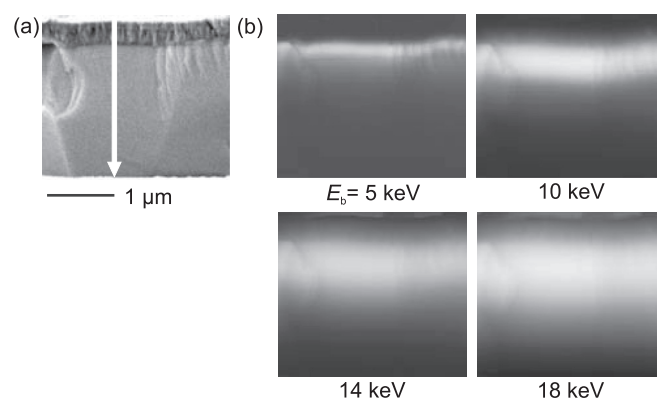


FIG. 3. SE image (a) and EBIC maps (b) for different electron beam energies E_b and for electron beam currents I_b in between 37 nA for $E_b = 5$ keV and 58 pA for 18 keV at the same position of a cross section of a CIGSe solar cell. The arrow marks the position where the EBIC profiles shown in Figure 4(a) were extracted.

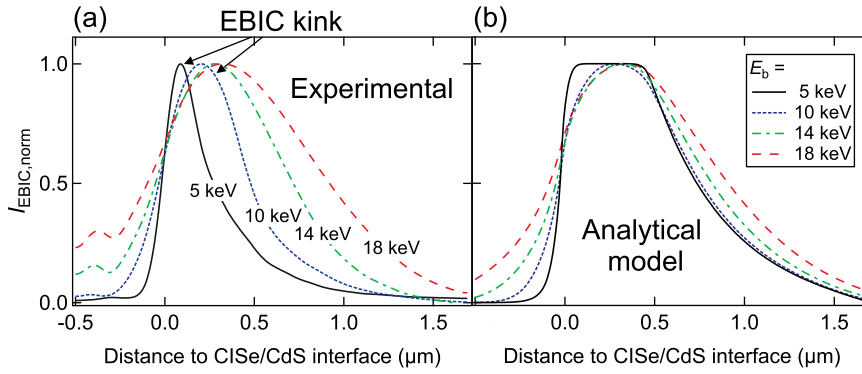


FIG. 4. Normalized measured (a) and calculated (b) EBIC profiles for different electron beam energies E_b . Parameters for analytical calculation: minority charge carrier diffusion lengths $L_{e,CISE} = 420$ nm, $L_{h,n-side} = 50$ nm, width of space charge region $w_{SCR} = 450$ nm and contact recombination velocities $S_C = 10^7$ cm/s at both contacts.

After, we will show EBIC profiles and corresponding numerical simulations of different grains of the absorber layer.

1. p+ layer (model A)

In Figure 5, three simulated EBIC profiles are shown for the standard set of parameters (i), for a p+ layer between the CISE and the CdS layer (ii), and for a p+ layer with a lowered valence band maximum with respect to the CISE layer (iii). The EBIC profile of the standard CISE solar cell (i) exhibits a broad maximum and a rather smooth decrease

towards the back contact. A p+ layer (ii) leads to a smaller width of the profile maximum, which is explainable by a reduced width of the space charge region. An EBIC kink, i.e., an abrupt decrease in current, is only present for a p+ layer with a lowered valence band maximum (iii). For the latter set of parameters (iii), which is denoted as model A in the following, the agreement between the measured and simulated EBIC profiles is good for all electron beam energies, which is shown in Figure 6(a).

TABLE III. Parameters for the simulation of the EBIC kink within models A, B1, B2, and C (Figure 6) and the IV curves for models A1, A2, A3, B1, B2, and C shown in Figure 11. All other parameters are as stated in Table I. IF1 denotes the CISE/CdS interface and IF2 the CdS/ZnO interface. The defect energies of the bulk defects are given with respect to the valence band maximum of the respective layer (E_V) and those of interface defects with respect to $E_{V,p+}$ at IF1 and $E_{V,CdS}$ at IF2. For the CISE layer, σ_e stands for the capture cross section of the midgap acceptor-type defect state.

| Model | A | A1 | A2 | A3 | B1 | | B2 | | C | |
|-------------------------------------|----------------------|---------------------|----------------------|---------------------|---------------------|---------------------|----------------------|----------------------|---------------------|---------------------|
| EBIC or IV? | EBIC | IV | IV | IV | EBIC | IV | EBIC | IV | EBIC | IV |
| CISE layer | | | | | | | | | | |
| σ_e (cm ²) | 2×10^{-14} | 2×10^{-15} | 2×10^{-15} | 2×10^{-15} | 2×10^{-14} | 2×10^{-15} | 2×10^{-14} | 2×10^{-15} | 2×10^{-14} | 2×10^{-15} |
| L_e (μm) | 0.51 | 1.6 | 1.6 | 1.6 | 0.51 | 1.6 | 0.51 | 1.6 | 0.51 | 1.6 |
| p+ layer | | | | | | | | | | |
| d_{p+} (nm) | 30 | 30 | 30 | 30 | ... | ... | ... | ... | ... | ... |
| $E_{g,p+}$ (eV) | 1.3 | 1.3 | 1.3 | 1.3 | ... | ... | ... | ... | ... | ... |
| $N_{t,p+}$ (cm ⁻³) | 1.5×10^{17} | 2×10^{17} | 2×10^{17} | 1×10^{17} | ... | ... | ... | ... | ... | ... |
| $E_{t,p+}$ (eV) | 0.5 | 0.5 | 0.5 | 0.5 | ... | ... | ... | ... | ... | ... |
| σ_e (cm ²) | 10^{-15} | 10^{-18} | 10^{-15} | 10^{-15} | ... | ... | ... | ... | ... | ... |
| σ_h (cm ²) | 10^{-13} | 10^{-12} | 10^{-13} | 10^{-13} | ... | ... | ... | ... | ... | ... |
| $\mu_{e,p+}$ (cm ² /Vs) | 4 | 4 | 4 | 4 | ... | ... | ... | ... | ... | ... |
| $\mu_{h,p+}$ (cm ² /Vs) | 1 | 1 | 1 | 1 | ... | ... | ... | ... | ... | ... |
| IF 1 | | | | | | | | | | |
| $N_{t,IF1}$ (cm ⁻²) | ... | 2×10^{11} | 2×10^{11} | 2×10^{11} | ... | 2×10^{11} | ... | 2×10^{11} | ... | 2×10^{11} |
| $E_{t,IF1}$ (eV) | ... | 1 | 1 | 1 | ... | 1 | ... | 1 | ... | 1 |
| CBO_{IF1} (meV) | 0 | 100 | 100 | 0 | 350 | Variable | 100 | 100 | 0 | 0 |
| CdS layer | | | | | | | | | | |
| $N_{t,CdS}$ (cm ⁻³) | ... | ... | 10^{17} | ... | 5×10^{16} | 5×10^{16} | 2.2×10^{17} | 2.2×10^{17} | ... | ... |
| $E_{t,CdS}$ (eV) | ... | ... | 1.2 | ... | 1.2 | 1.2 | 1.2 | 1.2 | ... | ... |
| σ_e (cm ²) | ... | ... | 10^{-15} | ... | 10^{-15} | 10^{-15} | 10^{-14} | 10^{-14} | ... | ... |
| σ_h (cm ²) | ... | ... | 10^{-13} | ... | 10^{-13} | 10^{-13} | 10^{-12} | 10^{-12} | ... | ... |
| $N_{d,CdS}$ (cm ⁻³) | 10^{16} | 10^{16} | 1.1×10^{17} | 10^{14} | 10^{16} | 10^{16} | 10^{17} | 10^{17} | 10^{16} | 10^{16} |
| $\mu_{e,CdS}$ (cm ² /Vs) | 4 | 4 | 4 | 4 | 40 | 40 | 40 | 40 | 40 | 40 |
| $\mu_{h,CdS}$ (cm ² /Vs) | 1 | 1 | 1 | 1 | 10 | 10 | 10 | 10 | 10 | 10 |
| IF 2 | | | | | | | | | | |
| $N_{t,IF2}$ (cm ⁻²) | ... | ... | ... | ... | ... | ... | ... | ... | 8×10^{11} | 8×10^{11} |
| $E_{t,IF2}$ (eV) | ... | ... | ... | ... | ... | ... | ... | ... | 1.8 | 1.8 |

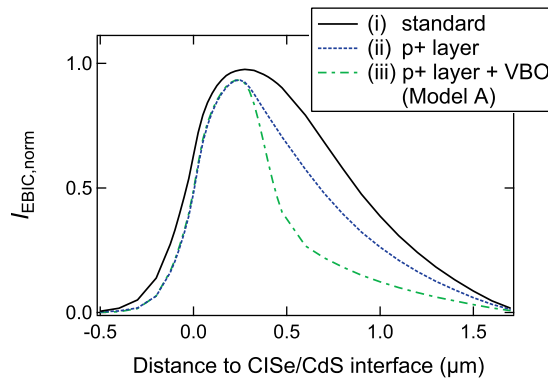


FIG. 5. Simulated EBIC profiles ($E_b = 10$ keV, $I_b = 10$ pA, $T = 300$ K) for: (i) standard CISE solar cell, i.e., no p+ layer (Table I), (ii) p+ layer ($E_{g,p+} = E_{g,CISE}$), (iii) model A: p+ layer with $E_{g,p+} = 1.3$ eV, valence band offset (VBO) between p+ layer and CISE.

The mechanism underlying generation-dependent transport in this model is a varying width of the space charge region in the absorber layer for different irradiation positions. This is shown by the electronic band diagrams in Figure 7(a). Under electron beam irradiation, the occupation of a deep defect state is governed by capture and emission of charge carriers according to the Shockley Read Hall theory.²⁸ The emission and capture rates depend on the local charge carrier densities, which in turn depend on the position of generation. Because of the high acceptor density in the p+ layer, the potential distribution across the pn-heterojunctions directly depends on the local electron and hole densities in the p+ layer. In equilibrium, the Fermi level is pinned at the acceptor energy. For generation far away from the p+ layer within the bulk of the CISE layer, the hole density in the p+ layer is low, because holes diffuse in direction of the back contact. Electrons move in direction of the heterointerface and are trapped into the acceptor-type defect state. Due to the high local negative charge density, the width of the space charge

region is small, and most of the potential drops in the n-type layers. If there is generation within the p+ layer, photo-generated holes are also trapped and reduce the negative charge density in the p+ layer, and the space charge region extends into the CISE layer. The EBIC kink within this model results from the fact that field assistance makes collection more efficient than pure diffusion in the quasi neutral region of the absorber layer. This is the case if the diffusion length is significantly smaller than the layer thickness. When moving the position of irradiation away from the CISE/CdS interface into the absorber layer, the position where the generation rate in the p+ layer gets too low resulting in a current decrease varies for different electron beam energies: the higher the electron beam energy, the broader is the generation profile, and the further away is this position from the CISE/CdS interface (see Figure 6(a)).

2. Deep acceptors in CdS (models B1 and B2)

We will now examine if the model of deep acceptor-type defects in the CdS and a conduction band spike at the CIGSe/CdS interface,^{3,6} i.e., a positive conduction band offset at IF1 (CBO_{IF1}), (denoted as model B1) can explain generation-dependent transport in EBIC. In Figure 8, simulated EBIC profiles are shown for different offset values. An EBIC kink is observed for a spike larger than 300 meV. The agreement of simulated and experimental data for different electron beam energies regarding the position of the EBIC kink, i.e., the position where the profiles decrease significantly, is good for a spike of 350 meV, which is shown in Figure 6(b). The electronic band diagrams for electron beam irradiation with and without generation in the CdS are shown in Figure 7(b). The effective barrier to overcome the conduction band spike depends on the value of the conduction band offset and the electron density at the CISE/CdS interface. It is larger for electron beam irradiation without

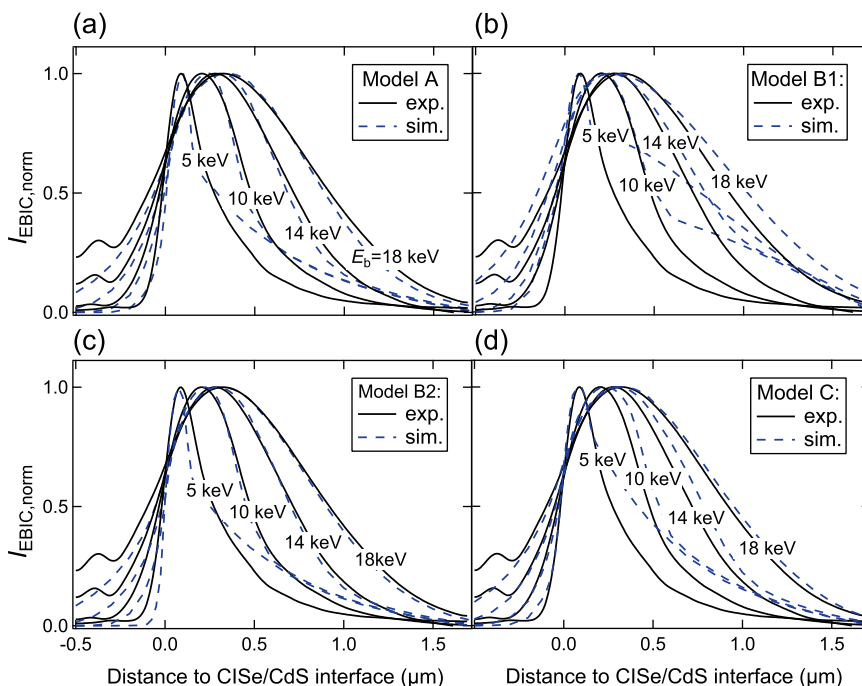


FIG. 6. Experimental (exp.) and simulated (sim.) EBIC profiles for different electron beam energies. (a) Model A as in Figure 5 (iii). (b) Model B1: midgap acceptors in CdS and a conduction band offset (spike, 350 meV) at the CISE/CdS interface (IF1). (c) Model B2: higher density of midgap acceptors in CdS and small conduction band spike at IF1 (100 meV). (d) Model C: acceptors at the CdS/ZnO interface.

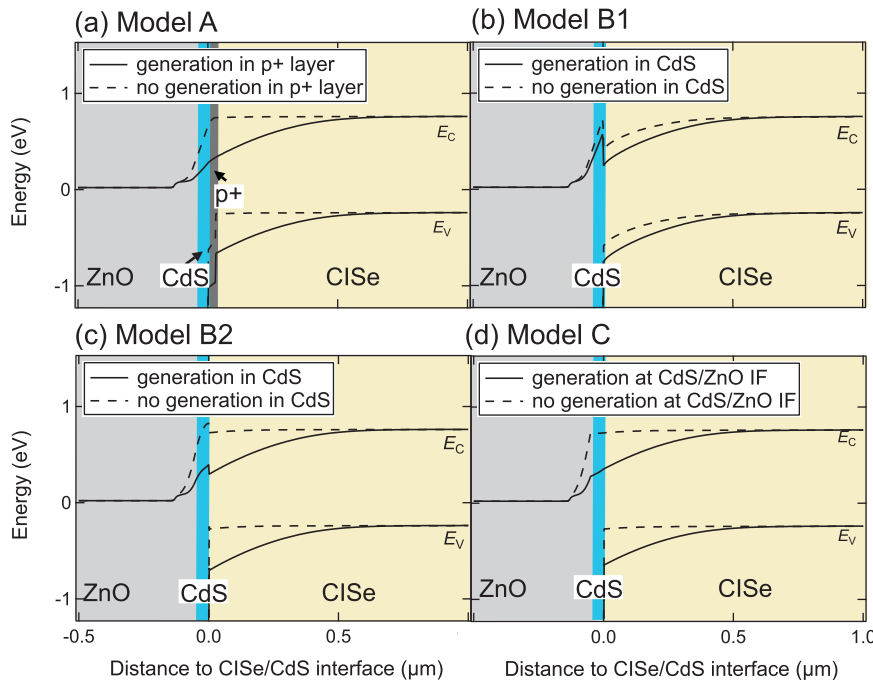


FIG. 7. Simulated electronic band diagrams of a CISE solar cell for different electron beam irradiation conditions ($E_b = 10$ keV, $I_b = 10$ pA) for the parameters of (a) model A, (b) model B1, (c) model B2, and (d) model C ($T = 300$ K).

generation in the CdS, which explains the occurrence of an EBIC kink.

If an even higher density of compensating acceptors in the CdS is assumed, its generation-dependent occupation probability can cause an EBIC kink without a large conduction band spike (denoted as model B2). This model is similar to that proposed by Hou *et al.*² to explain the red kink. Figure 6(c) shows that the agreement between the experimental and simulated data is good. In Figure 7(c), the electronic band diagrams for electron beam irradiation with and without generation in the CdS layer are shown. The main difference is the potential distribution throughout the device: without generation in the CdS, more potential drops in the CdS layer and the width of the space charge region within the CISE layer is smaller. Thus again, a varying width of the space charge region in the CISE layer causes the EBIC kink.

3. Acceptors at CdS/ZnO interface (IF2, model C)

A third model discussed in the literature to explain the red kink is that of acceptor-type defect states at the CdS/ZnO interface (denoted as model C).^{5,8} Corresponding simulated EBIC profiles are shown in Figure 6(d). The agreement between the experimental and simulated data is good. Again, a change in the width of the space charge region in the CISE layer caused by a generation-dependent occupation probability of the acceptor-type defect state at the CdS/ZnO interface is responsible for the occurrence of the EBIC kink. This is highlighted by the electronic band diagrams shown in Figure 7(d).

4. EBIC results for different grains

In Figure 9, a SE image (a) and an EBIC map (b) of two neighbouring grains of the absorber layer of a CISE solar cell are shown. Whereas the right grain appears completely bright

Model B1: Acceptors in CdS + spike at IF1

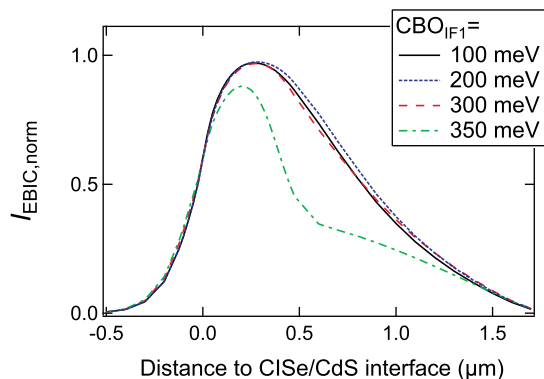


FIG. 8. Simulated EBIC profiles for the parameters of model B1 (deep acceptors in CdS with) and different values of the conduction band offset (spike, CBO_{IF1}) at the CISE/CdS interface. An EBIC kink occurs for a spike larger than 300 meV.

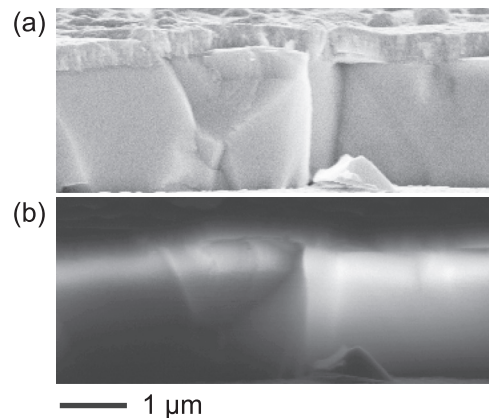


FIG. 9. SE image (a) and EBIC map (b) of a CISE solar cell for two different grains of the absorber layer ($E_b = 10$ keV). The significantly different EBIC signals in these two grains show that charge carrier transport is spatially inhomogeneous throughout the solar cell.

in the EBIC map, the left grain exhibits a narrow bright area located close to the pn-junction and appears rather dark in the quasi neutral region of the absorber layer. Thus, charge carrier transport is inhomogeneous throughout the absorber layer. In Figures 10(a) and 10(b), EBIC profiles of two other grains of the same absorber layer are shown for different electron beam currents in the range of 7 to 315 pA. At position 1, an EBIC kink occurs for all electron beam currents, whereas it is only observable for the highest value at position 2. For lower electron beam currents, the collection in the quasi neutral region is better. We find that the shape of EBIC profiles varies significantly in different grains of the absorber layer, whereas profiles from different positions in the same grain are normally similar. We conclude that the occurrence of generation-dependent charge carrier transport depends on the density of excess charge carriers. The critical density for the “onset” of generation-dependent transport is grain-specific.

We will now show that, within the model of a p+ layer, the assumption of an additional shallow interface donor at the p+ layer/CdS interface (IF1) can explain the observed dependence of the profile shape on the electron beam current displayed in Figures 10(a) and 10(b). For the profiles shown in Figure 10(c), only a p+ layer is assumed and the profile shape is the same for all electron beam currents. For the profiles shown in Figure 10(d), however, a donor-type defect state at the p+ layer/CdS interface, pinning the Fermi level at the interface close to the conduction band minimum, is assumed. The dependence of the EBIC profiles' shape on the electron beam current is similar to that of the measured ones shown in Figure 10(b). For this “intermediate” density of shallow interface donors, the occurrence of the EBIC kink depends on the occupation level of the donor for irradiation without generation in the p+ layer. The occupation in turn depends on the electron current from the CISE into the CdS

layer, i.e., on the density of generated charge carriers. For a small current density, the positive charge of the excited donor compensates the negative charge of the p+ layer and no EBIC kink occurs. For a higher current density, however, the donor state gets occupied by electrons to a higher degree. Its positive charge is not sufficient to compensate the negative charge trapped in the p+ layer. In consequence, the width of the space charge region in the CISE layer is smaller. This leads to reduced collection and an EBIC kink. The assumption of shallow interface donors at IF1 can also explain the observed dependence of the profile shape on electron beam current for models B1, B2, and C, which is shown in more detail in Ref. 27. Thus, a varying interface donor density at the interfaces of different CISE grains to CdS is a possible origin of grain-specific charge carrier transport.

C. IV characteristics

In Figure 11(a), red and white light illuminated IV curves measured at a temperature of 100 K are shown. While the fill factor of the white light illuminated IV curve is 80%, it is only 32% for red light illumination. A significant decrease in photocurrent under red light illumination and forward bias results in a poor fill factor and the characteristic “kink” shape of the curve, which is denoted as “red kink” effect. Generation conditions are different for red and white light illumination: while there is no generation in the CdS and ZnO layers for red light, white light contains high energy photons generating electron-hole pairs also in the n-type layers. The fact that a kink only occurs for red light means that charge carrier transport is generation-dependent. In this way, the red kink effect exhibits similarities to the EBIC kink introduced above. In Figure 11(b), the temperature dependence of the red light illuminated IV curves of the same

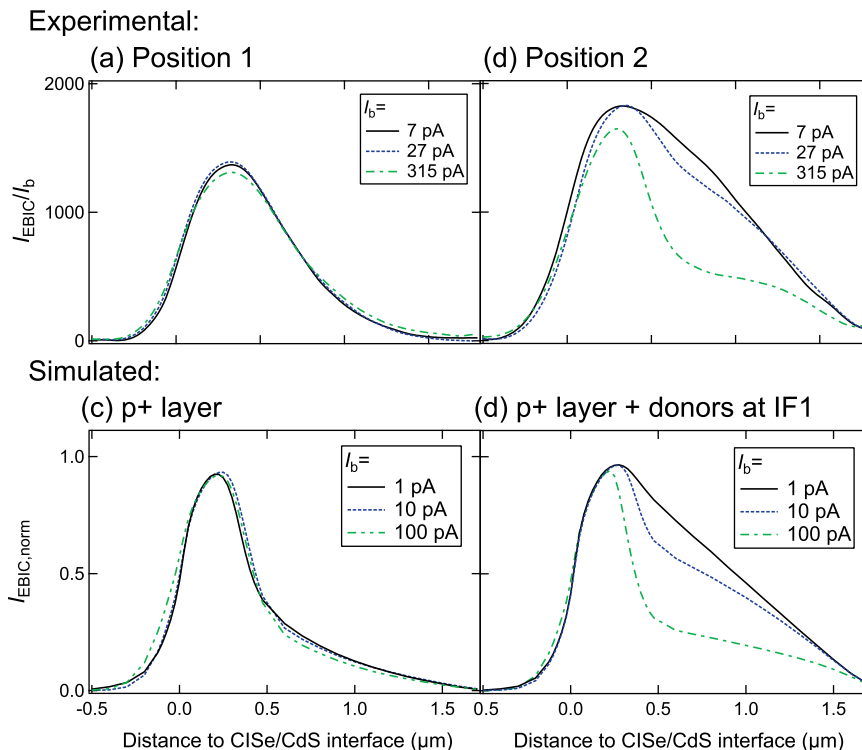


FIG. 10. (a) and (b) Measured EBIC profiles of two different grains for different electron beam currents I_b ($E_b = 10$ keV). (c) and (d) Simulated EBIC profiles for different electron beam currents I_b for (c) a p+ layer only (parameters as for curve (iii) in Figure 5) and (d) a p+ layer ($N_{L,p+} = 4 \times 10^{17} \text{ cm}^{-3}$) and a shallow interface donor at the CISE/CdS interface ($N_{L,IF1} = 10^{12} \text{ cm}^{-2}$, $E_{L,IF1} = E_{V,p+} + 1 \text{ eV}$). (To obtain better agreement, σ_e of the CISE midgap defect was changed to 10^{-15} cm^2 resulting in $L_{e,CISE} = 2.3 \mu\text{m}$ for the profiles shown in (d).)

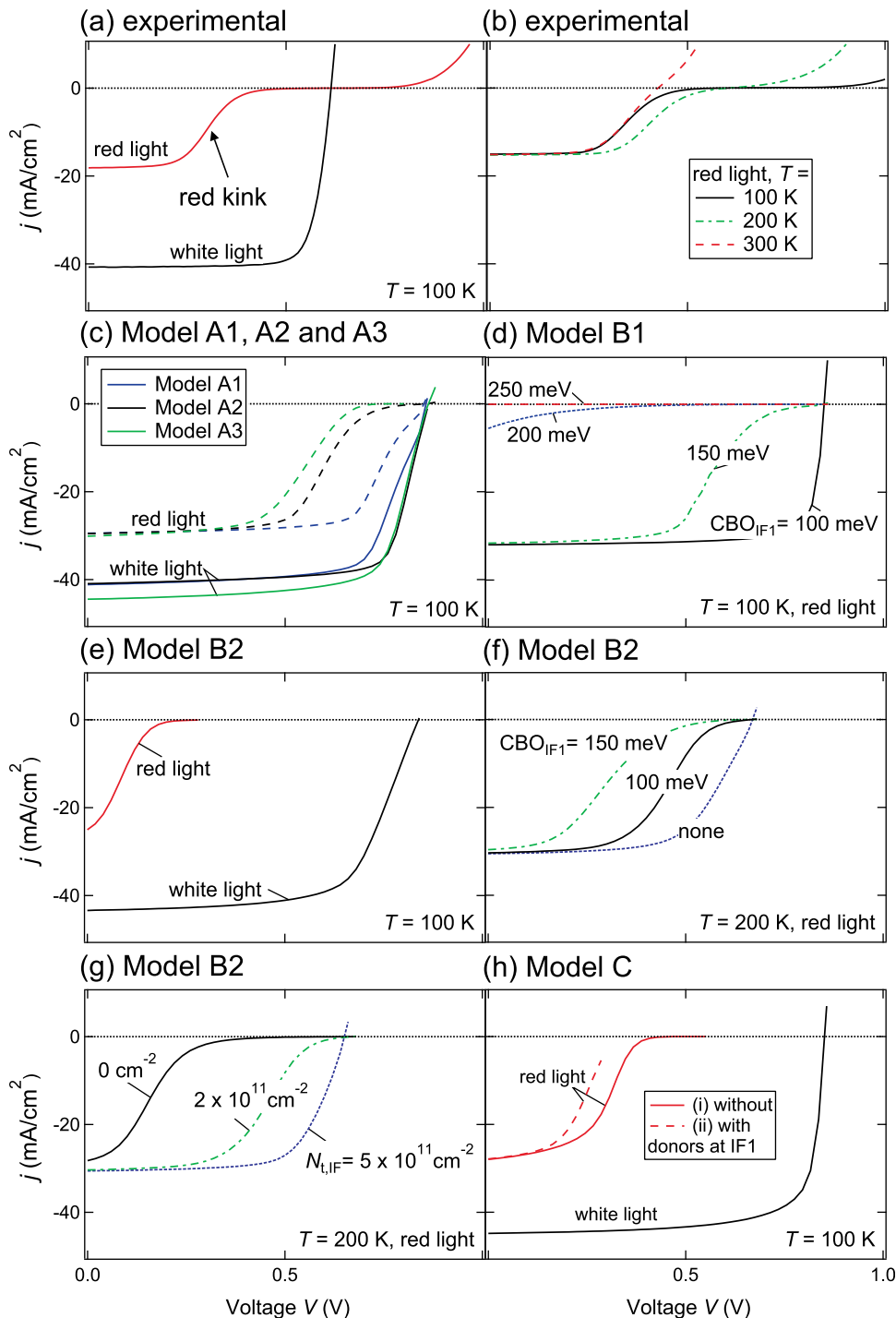


FIG. 11. (a) and (b) Measured IV curves of a CISE solar-cell for red and white light illumination at a temperature of 100 K (a) and for red light illumination at different temperatures (b). Simulated red and white light illuminated IV curves for $T = 100$ K or 200 K for: (c) Model A1: p+ layer only, model A2: p+ layer, acceptors in CdS and spike at the p+ layer/CdS interface (IF1), model A3: p+ layer and acceptors at the CdS/ZnO interface (IF2). (d) Model B1: Deep acceptors in CdS and conduction band spike at the CISE/CdS interface (IF1). (e) Model B2: Higher density of deep acceptors in CdS. (f) Model B2: Variation of conduction band offset at IF1 ($N_{t,IF1} = 2 \times 10^{11}$ cm⁻²). (g) Model B2: Variation of donor density at IF1 ($CBO_{IF1} = 100$ meV). (h) Model C: Acceptors at the CdS/ZnO interface (IF2).

solar cell is depicted. The lower the temperature, the more pronounced is the red kink effect and the smaller is the fill factor.

For the simulations of IV data at low temperatures, we have to take into account that charge-carrier transport properties are inhomogeneous with respect to the occurrence of the EBIC kink and the electron diffusion length in CISE. (The corresponding results concerning the electron diffusion length are not shown here, for details refer to Ref. 27.) In contrast to EBIC, an IV measurement provides integral information. It is, therefore, necessary to use estimated average values for the simulation of IV curves. All sets of parameters used for the IV simulations shown in the following yield

good agreement of the experimental and simulated EBIC data (without donor-type defect states at IF1). Details on the simulations parameters are summarized in Table III.

1. Models A1, A2, and A3

In the following, we will discuss the simulations of IV curves at low temperatures using sets of parameters including a p+ layer with a lowered valence band maximum as the origin of the EBIC kink. The origin of the red kink effect is either assumed to be given by the p+ layer (model A1), acceptors in the CdS and a conduction band spike at the CISE/CdS interface (IF1, model A2), or acceptors at the

CdS/ZnO interface (IF2, model A3). The simulated IV curves for these three models are displayed in Figure 11(c).

Our simulations of IV curves yield higher V_{OC} values than measured. A possible explanation for this discrepancy is given by a non-Ohmic CISE/Mo back contact. It was shown that a back contact barrier can cause a saturation of V_{OC} for low temperatures.²⁹ We do not include such a non-Ohmic back contact in our simulation parameters because it leads to convergence failures of the simulation algorithm. We neglect the discrepancy in V_{OC} between the experimental and simulated IV curves and focus only on the red kink effect at low temperatures, i.e., the curve shape and the difference in fill factor between red and white light illuminated IV curves.

For model A1 (p+ layer only, blue curves in Figure 11(c)), there is a difference in fill factor between red and white light illuminated IV curves, but it is not as pronounced as observed experimentally. Due to strongly asymmetric capture cross sections for electrons and holes ($\sigma_h/\sigma_e = 10^6$) and differences in hole densities in the p+ layer, there is a difference in occupation probability of the acceptor of the p+ layer for red and white light illumination. This results in a difference in fill factor between red and white light illuminated IV curves. However, in contrast to an EBIC experiment, in which it is possible to generate only in the bulk of the CISE layer, there is generation in the p+ layer for red and for white light illumination. Consequently, the difference in space charge distribution for red and white light illumination is not sufficient to cause fill factor losses for red light as observed experimentally. It is possible to obtain better agreement between the measured and simulated IV curves if a shallower defect ($E_{t,p+} = E_{v,p+} + 150$ meV) is assumed, but for the simulation of EBIC data, a deep defect is required. We conclude that the assumption of a p+ layer only is not sufficient to simulate EBIC and IV data consistently.

In model A2 (black curves in Figure 11(c)), the model of a p+ layer with a lowered valence band maximum, deep acceptor-type defect states in the CdS, and a conduction band spike at the p+ layer/CdS interface (IF1) were combined. While the p+ layer is the origin of an EBIC kink at room temperature, the conduction band spike serves as a current barrier at 100 K under forward bias and red light illumination resulting in a red kink as in Eisgruber's model.³ Within this approach, the origins of the phenomena observed in EBIC and IV are different. Good qualitative agreement between the experimental and simulated data is obtained. Another possible combination of models is that of a p+ layer with a lowered valence band maximum as origin of the EBIC kink and acceptor-type defect states at the CdS/ZnO interface (IF2) to be responsible for a red kink (denoted as model A3, green curves in Figure 11(c)). Again, the origins of the effects in EBIC and IV are different and the qualitative agreement between the experimental and simulated data is good.

We conclude from these simulations that a consistent explanation of generation-dependent transport in EBIC and IV is not possible with the assumption of a p+ layer only, but by assuming acceptor-type defect states at the CdS/ZnO interface or within the CdS in addition to a p+ layer.

2. Models B1 and B2

In Figure 11(d), simulated red light illuminated IV curves are shown for acceptor-type defect states in the CdS and a conduction band spike at the CISE/CdS interface (model B1) for different values of the conduction band offset at the CISE/CdS interface (IF1). The current in the forward bias range is smaller, the larger is the offset. It is in the $\mu\text{A}/\text{cm}^2$ range for an offset value of 250 meV, which is in contrast to the experimental observations. We have shown before that an EBIC kink occurs for offset values larger than 300 meV. Since the thermionic emission current across an energetic barrier depends exponentially on temperature, a temperature-independent barrier cannot be the origin of generation-dependent transport observed in EBIC and IV simultaneously. Thus, it is not possible to explain the red kink and the EBIC kink consistently within model B1, which is why we do not consider it further.

In Figure 11(e), IV curves simulated for a temperature of 100 K are shown for the same set of parameters as used for the simulation of EBIC profiles shown in Figure 6(c) (model B2: even higher acceptor density in CdS and a small conduction band spike at IF1). With this set of parameters, the red kink is more pronounced and the fill factor of the white light illuminated IV curve is smaller than observed experimentally. For the simulated IV curves shown in Figures 11(f) and 11(g), for which additional shallow donors at the CISE/CdS interface were assumed, a temperature of 200 K was assumed because of convergence problems of the simulation algorithm for 100 K. The qualitative trends of the parameter variations shown in the following are transferable to lower temperatures. In Figure 11(f), a varying conduction band offset (spike) at the CISE/CdS interface (IF1) was assumed. The larger the conduction band spike, the more pronounced is the red kink effect due to a larger barrier for the electron current from the absorber layer into the CdS according to thermionic emission theory. For the simulations shown in Figure 11(g), a varying interface donor density at IF1 was assumed. The presence of the positive interface charge of the excited donor state reduces the extent of the red kink. These simulations indicate that a consistent explanation of EBIC and IV data within model B2 is possible for a spike significantly smaller than 100 meV (or even flatband alignment or a conduction band cliff) and shallow interface donors at the surface of those CISE grains, which do not exhibit an EBIC kink.

3. Model C

In Figure 11(h), simulated red and white light illuminated IV curves for a temperature of 100 K and a solar cell with acceptor-type defect states at the CdS/ZnO interface (IF2) without (i) and with (ii) additional donors at the CISE/CdS interface (IF1) are shown. The presence of donor-type interface states at IF1 increases the extent of the red kink. This is due to the pinning of the Fermi level at both interfaces and the resultant field inversion within the CdS layer, which constitutes a barrier for the electron current if there is not enough thermal energy at low temperatures. The extent of the red kink effect, i.e., the difference in fill factor

between red and white light illuminated IV curves, is more pronounced than observed experimentally with and without interface donors at IF1. Thus, a consistent explanation of generation-dependent transport in EBIC and IV is not possible on a quantitative level by assuming acceptor-type defect states at the CdS/ZnO interface. For a realistic simulation of the red kink effect, a lower interface defect density has to be assumed than for the simulation of an EBIC kink. A spatially varying acceptor defect density at the CdS/ZnO interface could, in principle, account for the deviations between the simulated and measured data. However, since the inhomogeneities with respect to the EBIC kink are grain specific for grains of the absorber layer, this possibility is not likely. We do not consider model C further in this publication.

D. Variation of the CdS thickness

The dependence of the red kink on electrical properties of the CdS is different for the models discussed in the literature. For a variation of the CdS layer thickness, the number of the defects directly responsible for the red kink varies only for the models of acceptor-type defect states in the CdS layer.^{2,3} In consequence, a CdS thickness variation is expected to have the most pronounced influence for models B1 and B2. We performed IV measurements on a series of CISE solar cells with different CdS layer thicknesses in order to distinguish between the models for the red kink. The room

temperature solar cell parameters and absorber layer compositions are given in Table II. The normalized red light illuminated IV curves of these solar cells at a temperature of 100 K are shown in Figure 12(a). The larger the CdS thickness, the more pronounced is the red kink effect.

In Figures 12(b)–12(e), simulated red light illuminated IV curves for the models A1, A2, A3, and B2 are shown for different CdS layer thicknesses. For the set of parameters assuming a high density of deep acceptor-type defect states in the CdS (model B2), a temperature of 200 K was assumed, again because of convergence problems of the simulation algorithm for a temperature of 100 K. For the simulation of equivalent red kink effects at a temperature of 100 K, the spike height (100 meV for 200 K) would have to be reduced.

The CdS layer thickness influences the red kink in all three models. The agreement between the simulated and measured data is best for the model of a p+ layer only (model A1, Figure 12(b)) and a p+ layer, midgap acceptors in the CdS and a conduction band spike at the CISE/CdS interface (model A2, Figure 12(c)). For the model of a p+ layer and acceptor-type defect states at the CdS/ZnO interface (model A3, Figure 12(d)), the dependence of the red kink on the CdS thickness is less pronounced than observed experimentally. The assumption of a high density of deep acceptors in the CdS only (model B2, Figure 12(e)) leads to a strong deviation between the measured and simulated IV curves for a layer thickness of 120 nm. The photocurrent is

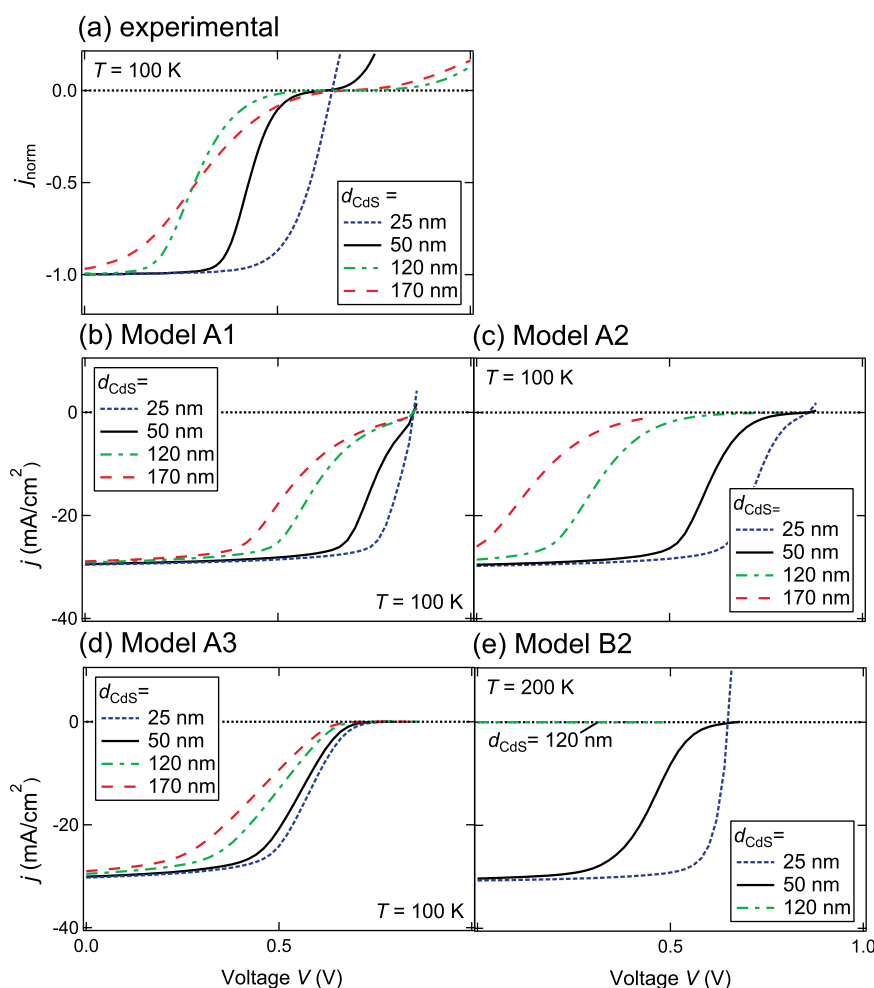


FIG. 12. (a) Measured normalized red light illuminated IV curves of CISE solar cells with different CdS layer thicknesses d_{CdS} for $T = 100$ K. (b)–(e) Simulated red light illuminated IV curves for (b) model A1: p+ layer only, $T = 100$ K (c) model A2: p+ layer, acceptors in CdS, a conduction band spike at IF1, $T = 100$ K, (d) model A3: p+ layer, acceptors at IF2, $T = 100$ K, and (e) model B2: high density of acceptors in CdS, $T = 200$ K.

significantly reduced (to some $\mu\text{A}/\text{cm}^2$) in the full range of forward bias, which is independent of the assumed value of the conduction band spike and only caused by the high amount of negative charge within the CdS layer and the resulting field inversion. Due to these significant deviations between the experimental and simulated data, we exclude model B2.

E. Variation of the Ga-content of the absorber layer

In the following, we will discuss the influence of the conduction band offset at the CIGSe/CdS interface (IF1) on the red kink effect. In CIGSe/CdS solar cells, the spike height can be varied by a variation of the Ga-content of the absorber layer at the interface: with increasing local Ga-content, the conduction band shifts upwards.³⁰ Generally, it is assumed that the conduction band offset changes with increasing Ga-content from a small spike for the CuInSe₂/CdS interface to a cliff configuration for higher Ga-contents.^{30,31} In this publication, a spike, i.e., if the conduction band minimum on the CdS side of the junction is at a higher energy level, is defined as a positive conduction band offset and a cliff as a negative one. Pudov *et al.*⁶ showed that there is indeed a correlation between the Ga-content and the extent of the red kink occurring at room temperature for their solar cells. They showed that their results are in good agreement with the model assuming deep acceptor-type defect states in the CdS and a conduction band spike at the CIGSe/CdS interface, which was introduced by Eisgruber *et al.*³ In their study, however, solar cells with absorber layers deposited in a single-stage coevaporation process were used, which might exhibit significant differences in junction properties. We performed IV measurements on a series of CIGSe solar cells with absorber layers of varying Ga-content in order to evaluate the dependence of the red kink at low temperatures on the conduction band offset at the CIGSe/CdS interface in our solar cells with absorber layers deposited in a multistage process. We will also show numerical simulations for models A1, A2, and A3, i.e., for different origins of the red kink effect, and compare them to our experimental results.

In absorber layers deposited in a multistage coevaporation process as explained in Sec. II A, the local Ga to In ratio and consequently the bandgap energy are not constant throughout the depth of the absorber layer.²¹ To determine the local Ga-content at the CIGSe surface (=CIGSe/CdS interface), we performed energy dispersive x-ray (EDX) measurements on cross sections of the absorber layers containing In and Ga (results not shown here, refer to Ref. 27). In Table IV, the Ga-content at the CIGSe surface obtained from a linear fit of EDX linescans and normalization to the integral Ga-content as determined by means of x-ray fluorescence and the corresponding surface bandgap energies (bowing coefficient: $b = 0.15$) are given. The conduction band offset at the CIGSe/CdS interface varies significantly for these solar cells ($\Delta\text{CBO} = 220\text{ meV}$ for the solar cells with absorber layers with Ga/III = 0 and 0.5).

In Figures 13(a) and 13(b), measured red and white light illuminated IV curves for a temperature of 100 K are shown. Note that all profiles are normalized to the current density for a voltage of $V = -0.1\text{ V}$ to make the extent of the red

TABLE IV. Integral Ga content as determined by XRF, Ga-content at the absorber layer surface (SF = CIGSe/CdS interface) as determined by EDX and calculated absorber surface bandgap energy of the absorber layers of the solar cells used for IV measurements. The bandgap energies for Ga/III = 0 and 1 were assumed to be 1.04 eV and 1.68 eV.

| Solar cell | Ga/III | Ga/III _{SF} | E _{g,SF} (eV) |
|--------------|--------|----------------------|------------------------|
| Ga/III = 0.3 | 0.34 | 0.28 | 1.19 |
| Ga/III = 0.5 | 0.50 | 0.40 | 1.26 |
| Ga/III = 0.7 | 0.73 | 0.64 | 1.42 |

kink comparable. A red kink only occurs for the samples with a Ga-content up to Ga/III = 0.5. The solar cell with an absorber layer of Ga/III = 0.7 exhibits a kink in both red and white light illuminated IV curves. The CuGaSe₂ solar cell has a low fill factor for red and white light illumination, but the curve shape is not that of the typical kink feature. For the samples with low Ga-content (Ga/III \leq 0.5), there is no unambiguous trend with respect to the extent of the red kink, i.e., difference in fill factor between red and white light illuminated IV curves, for an increasing Ga-content (Figure 13(a)). The red kink is more pronounced for Ga/III = 0.5 than for Ga/III = 0 and 0.3.

In Figures 13(c) to 13(h), simulated IV curves for different values of the conduction band spike at the CIGSe/CdS interface (IF1) are shown for the parameters of models A1, A2, and A3. These three models all include a p+ layer as the origin of the EBIC kink but different mechanisms for the red kink effect: p+ layer (model A1), acceptors in the CdS and a conduction band spike at IF1 (model A2), and acceptors at the CdS/ZnO interface (IF2, model A3). A CIGSe absorber layer with a bandgap energy of 1 eV was assumed and the conduction band offset at the CIGSe/CdS interface was adjusted solely by changing the electron affinities of the n-type layers. Thus, our simulations do not reflect a real variation of the Ga-content of the absorber layer, because in this case, a Ga-gradient and other parameters variations would have had to be included as well. The focus is on an investigation of the influence of the conduction band offset at the CIGSe/CdS interface on a qualitative level.

A change in conduction band spike (positive conduction band offset) of only 20 to 60 meV has a significant influence on the red kink for all three models (Figures 13(c), 13(e), and 13(g)). For flatband alignment, there is no red kink for models A1 and A2 and the fill factor of red and white light illuminated IV curves is largest (Figures 13(d) and 13(f)). A cliff configuration leads to a reduced open circuit voltage for red and white light illumination, which is explainable by enhanced recombination in the heterojunction region due to a reduced hole barrier at the interface. For model A3, there is a red kink for flatband alignment and a cliff configuration (Figure 13(h)). The open circuit voltage is again reduced for a cliff. An offset of -200 meV leads to a more pronounced red kink than a cliff of -300 meV . We could not perform simulations assuming a larger cliff than -300 meV because of convergence problems of the simulation algorithm.

It is not possible to explain our experimental results unambiguously with these simulations. A variation of the

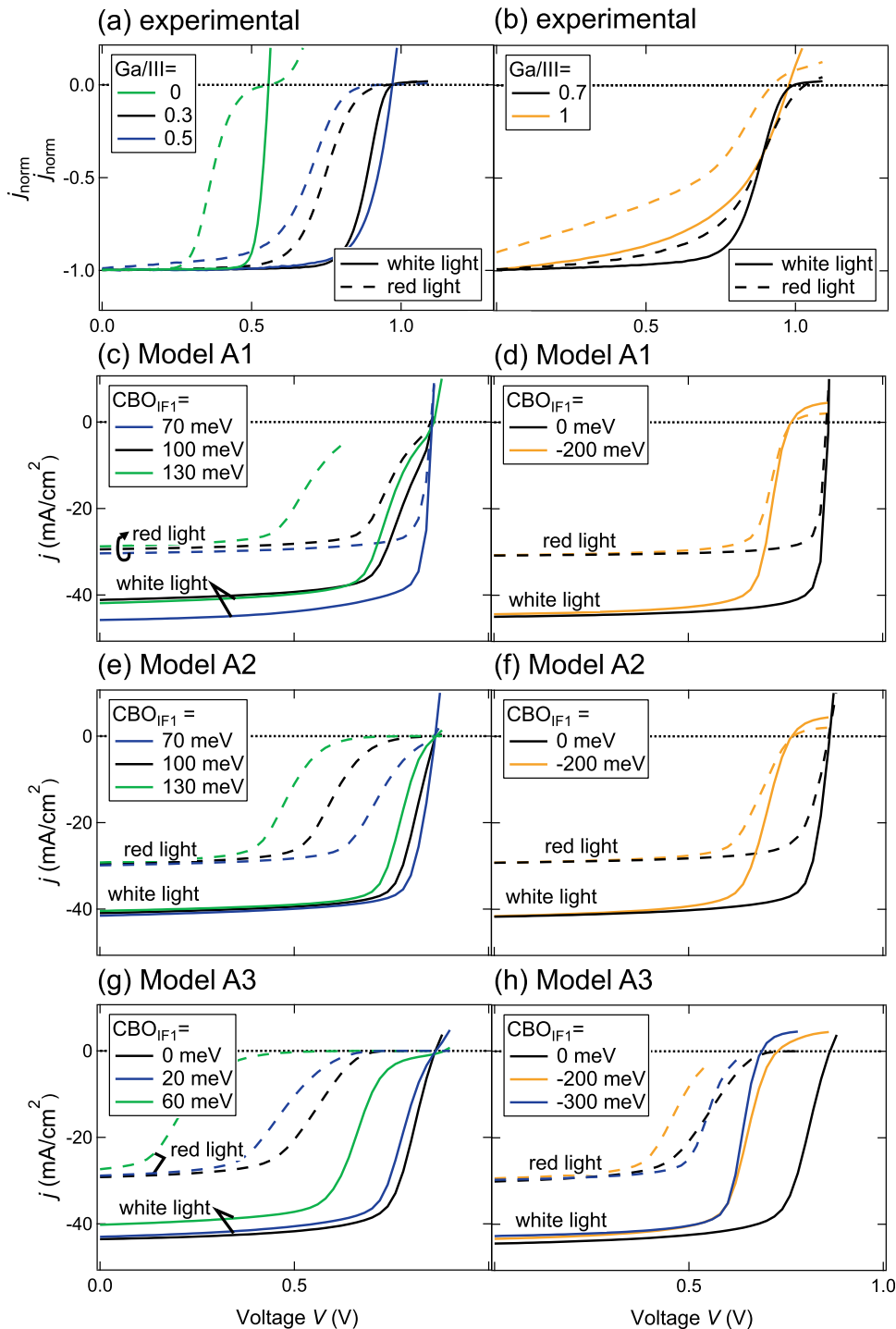


FIG. 13. (a) and (b) Normalized experimental red (dashed lines) and white (solid lines) light illuminated IV curves of a series of solar cells with absorber layers of varying Ga-content, $T = 100$ K ((a) $\text{Ga/III} = 0, 0.3$, and 0.5 (b) $\text{Ga/III} = 0.7$ and 1), (c) to (h) Simulated red and white light illuminated IV curves at $T = 100$ K for different values of the conduction band offset at the CISE/CdS interface (IF1) for models A1, A2, and A3.

Ga-content of the absorber layer has a complex influence on the absorber layer and consequently the solar cell: defect and doping densities, the microstructure and grain boundaries and interface properties might be affected significantly. All these can have a major impact on the fill factor at low temperatures. For models A1 and A2, there is no agreement between the experimental and simulated data: there is only a red kink for a spike configuration at the CISE/CdS interface and the larger the spike, the more pronounced is the red kink effect. The best explanation of our experimental data with respect to the red kink is given by the parameters of model

A3 (p+ layer and acceptors at the CdS/ZnO interface (IF2)) assuming a small spike or flatband alignment at the CISE/CdS interface (IF1) for the CISE solar cell. The simulations show that a cliff of -200 meV does not affect the extent of the red kink significantly. An increase of the absorber-layer surface bandgap-energy by 220 meV as for the sample with $\text{Ga/III} = 0.5$ would imply a cliff in this order of magnitude. This solar cell exhibits a similar red kink as the CISE solar cell (Figure 13(a)), which is consistent with the simulations for the parameters of model A3. For an even larger cliff of -300 meV, the simulated red kink is less pronounced,

i.e., the difference between the fill factors of the red and white light illuminated IV curves is smaller. This is consistent with the fact that the solar cells with an absorber layer of Ga/III = 0.7 exhibits only a small difference in fill factor between red and white light illuminated IV curves (Figure 13(b)).

IV. DISCUSSION

The results of our numerical simulations are summarized in Table V. We can draw the following conclusions about the origin of generation-dependent charge carrier transport in EBIC and IV from the results presented in this work.

Origin of the EBIC kink. We can only explain our results consistently by assuming a p+ layer with deep acceptor-type defect states and a lowered valence band maximum (model A) as the origin of generation-dependent transport in EBIC. We exclude the model introduced by Eisgruber *et al.* (model B1), because a conduction band spike at the CIGSe/CdS interface cannot simultaneously cause a current decrease in EBIC at room temperature and in IV at low temperatures. The assumption of a high density of acceptor-type defect states in the CdS (model B2) leads to significant deviations between the simulated and experimental IV characteristics of a series of solar cells with varying CdS thickness as shown in Figure 12(e). Slight deviations would be explainable by a varying interface donor density for different CdS thicknesses due to interdiffusion during chemical bath deposition (e.g., Cd_{Cu} defects³²) or an inhomogeneous acceptor distribution in the CdS with a maximum close to the CIGSe/CdS interface. But since the observed deviations are immense, we exclude this model. We also exclude acceptor-type defect states at the CdS/ZnO interface (model C) as an explanation for the EBIC kink because of discrepancies between the simulated IV and EBIC data on a quantitative level.

Origin of the red kink. Our results indicate that a p+ layer alone cannot be the origin of a red kink (model A1). The simulations yield less pronounced fill factor deficiencies under red light illumination than observed experimentally in our study if a p+ layer with a deep defect capable of explain-

ing an EBIC kink is assumed. This is in contrast to the model suggested by Igalson *et al.*^{4,13,17} The results of a series of solar cells with absorber layers of varying Ga-content indicate that the conduction band spike at the p+ layer/CdS interface does not serve as a photocurrent barrier at low temperatures resulting in a kink in the IV curve (model A2). There is no correlation between the absorber layer surface bandgap energy and the extent of the red kink. This is in contrast to the findings of Pudov *et al.*⁶ Another difference between their and our results is that we observe a red kink only at low temperatures, whereas they observe it for low Ga-contents also at room temperature. Since their absorber layers are deposited in a single-stage coevaporation process possibly leading to different electronic properties of the absorber bulk and of the absorber/buffer interface, the red kink might have different origins in their solar cells and in ours. Our results from solar cells with absorber layers of higher Ga-contents (Ga/III = 0.7 and 1) also indicate that (red) kinks or fill factor deficiencies in general, have multiple origins. In spite of slight deviations between the experimental and simulated IV curves for the solar cells with varying CdS layer thickness, the model of a p+ layer to be responsible for the EBIC kink and acceptor-type defect states at the CdS/ZnO interface for the red kink (model A3) provides the best explanation of generation-dependent transport in EBIC and IV on a quantitative level. This model combines models A and C. It is also possible that a combination of acceptor-type defect states located at the CdS/ZnO interface and within the CdS causes the red kink. In principle, our model can also explain metastable variations of the red kink effect and the negative charge density upon a voltage bias or light soaking as reported in Refs. 13 and 17. This will be the subject of future work.

One requirement for the explanation of an EBIC kink with a p+ layer is the assumption of a valence band offset between the p+ layer and the CIGSe layer. In earlier studies, it was found that a vacancy compound (VC) forms at the surface of Cu-poor CIGSe layers³³ (in Ref. 33, the VC layer is denoted as ordered defect compound (ODC)). A bandgap energy of approximately 0.3 eV larger than that of the corresponding CIGSe layer was determined. The assumption of a VC layer at the CIGSe/CdS interface questions the model of ($V_{\text{Se}} - V_{\text{Cu}}$) defect complexes and In_{Cu} antisite defects as suggested by Lany and Zunger^{14,15} to be the origin of a high negative charge density in the interface region of the solar cell.¹⁶ Their calculations and conclusions are based on CuInSe_2 and not the structure of a vacancy compound with an enlarged bandgap energy. In contrast to our assumption of a highly p-doped VC layer, EBIC and spectral response data of a Mo/CIGSe/VC/Al structure shown in Ref. 11 led to the conclusion that the VC layer is weakly n-type. Whereas the maximum of the EBIC profile shown in Ref. 11 is located deep in the bulk of the absorber layer indicating n-type conductivity of the VC layer and a buried junction, our EBIC profiles exhibit a maximum close to the heterojunction. This indicates differences in junction formation between the solar cells used in their study, which have absorber layers deposited in a single-stage coevaporation process, and ours. One major difference might consist in Na-incorporation in the absorber

TABLE V. Summary of the conclusions drawn from the numerical simulation of EBIC and IV characteristics of CIGSe solar cells, CIGSe solar cells with different CdS layer thicknesses and CIGSe solar cells with absorber layers of varying Ga-content. “Yes” and “No” mean that the respective model does or does not explain the experimental data. “not consistent” means that there is no consistent set of parameters for a simulation of IV and EBIC data within the respective model. “...” means that the respective simulations are not shown in the present publication, because they are not relevant.

| Model | EBIC kink CuInSe ₂ | Red kink CuInSe ₂ | Red kink CdS-series | Red kink Ga-series |
|----------|----------------------------------|---------------------------------|------------------------|-----------------------|
| Model A1 | Yes | To some extent | Yes | No |
| Model A2 | Yes | Yes | Yes | No |
| Model A3 | Yes | Yes | Yes | Yes |
| Model B1 | Yes | Yes | ... | ... |
| | Not consistent | | | |
| Model B2 | Yes | Yes | No | ... |
| Model C | Yes | Yes | ... | ... |
| | Not consistent | | | |

layer. This would have a major impact on the local charge carrier density because Na is found to increase the net p-type doping density in CIGSe³⁴ and also in the vacancy compound CuIn₃Se₅.³⁵

Another important finding of this work is that charge carrier transport is spatially inhomogeneous throughout the solar cell. These grain-specific differences can be explained consistently by a donor-type interface defect at the p+ layer/CdS interface of some grains of the absorber layer. In Ref. 32, the occupation of Cu sites by Cd was found to form a shallow donor state. The assumption that there are orientation dependent differences in diffusion properties of Cd in CIGSe as suggested in Ref. 36 provides an explanation for the inhomogeneities. An electronic band diagram of the model we suggest is displayed in Figure 14.

In contrast to our assumptions, Kniese *et al.*¹ suggested donor-type defect states at the p+ layer/CdS interface in addition to a p+ layer with a lowered valence band maximum as an explanation of the EBIC kink. A donor is not a necessary component in our model to explain the EBIC kink, but to explain the fact that it occurs only for high electron beam currents in some grains of the absorber layer. Kniese *et al.*¹ assume a larger capture cross section for holes than for electrons of this donor-type defect state. This is different from what we assume and in contrast to the usual assumption that a positively charged donor has a larger capture cross section for electrons due to electrostatic attraction.

In order to identify the influence on solar cell performance, we performed simulations of white light illuminated IV curves at 300 K, which are shown and discussed in more detail in Ref. 27. We find that the assumption of a lowered valence band maximum in the region of the absorber layer close to the interface has a positive effect on device performance. The hole density in this region and hence recombination are reduced.³⁷ The presence of a p+ layer has a slightly positive effect on the open circuit voltage due to its high space charge density. A homogeneous intermediate density of donor-type defect states at the p+ layer/CdS interface would improve the fill factor. If the density is too high and the Fermi level is pinned at the CIGSe/CdS interface, field inversion in the CdS can occur if there is also Fermi level pinning at the CdS/ZnO interface.⁸ This has a negative effect

on charge carrier transport. Acceptor-type defect states at the CdS/ZnO interface of a density of $N_{IF2} = 8 \times 10^{11} \text{ cm}^{-2}$, as assumed for our simulations, do not influence device performance significantly.

V. CONCLUSIONS

In this work, a combination of cross-section EBIC measurements and illumination-dependent IV measurements in conjunction with numerical simulations was used to develop a consistent model for the heterojunction region of CIGSe/CdS/ZnO solar cells with absorber layers deposited in a multistage evaporation process of low Ga-content ($\text{Ga/III} \leq 0.35$) (see Figure 14). Experimental results and simulations indicate that generation-dependent charge carrier transport in EBIC and IV experiments has different microscopic origins. A thin ($\approx 30 \text{ nm}$) p+ layer between the CIGSe and the CdS layers with a high density of deep acceptor-type defect states (in the range of $N_{t,p+} \approx 10^{17} \text{ cm}^{-3}$) and a lowered valence band maximum is suggested to serve as the origin of generation-dependent transport in EBIC. On the other hand, the red kink effect in IV characteristics results from acceptor-type defect states at the CdS/ZnO interface in our model. An explanation for spatial inhomogeneities, i.e., grain-specific charge-carrier transport properties, observed in EBIC is given by a varying density of donor-type defect states at the p+ layer/CdS interface.

ACKNOWLEDGMENTS

The authors would like to thank J. Bundesmann, T. Münchenberg, J. Liebich, and J. Schniebs for technical support and U. Rau, S. Schmidt, and T. Eisenbarth for fruitful discussions.

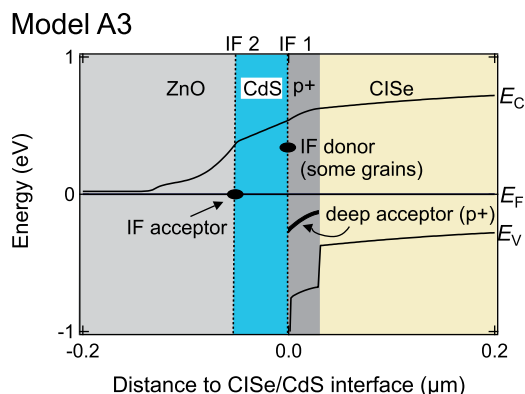


FIG. 14. Detail sketch of the electronic band diagram of a CIGSe solar cell according to the parameters of model A3, which is capable of explaining the experimental IV and EBIC data of this study consistently.

- ¹R. Kniese, M. Powalla, and U. Rau, *Thin Solid Films* **515**, 6163 (2007).
- ²H. Hou, S. Fonash, and J. Kessler, in *Conference Record of the Twenty Fifth IEEE Photovoltaic Specialists Conference* (1996), p. 961.
- ³I. Eisgruber, J. Granata, J. Sites, J. Hou, and J. Kessler, *Sol. Energy Mater. Sol. Cells* **53**, 367 (1998).
- ⁴M. Igalson, P. Kubiacyk, and P. Zabierowski, *Mater. Res. Soc. Symp. Proc.* **668**, H9.2.1 (2001).
- ⁵M. Topic, F. Smole, and J. Furlan, *Sol. Energy Mater. Sol. Cells* **49**, 311 (1997).
- ⁶A. Pudov, A. Kanevce, H. Al-Thani, J. Sites, and F. Hasoon, *J. Appl. Phys.* **97**, 064901 (2005).
- ⁷Y. Lee and J. Gray, in *IEEE First World Conference on Photovoltaic Energy Conversion/Conference Record Of The Twenty Fourth IEEE Photovoltaic Specialists Conference* (1994), Vols. I–II, p. 287.
- ⁸A. Urbaniak and M. Igalson, *Mater. Res. Soc. Symp. Proc.* **1165**, 9 (2010), available at: <http://journals.cambridge.org/action/displayAbstract?fromPage=online&aid=7969312>.
- ⁹D. Liao and A. Rockett, *J. Appl. Phys.* **93**, 9380 (2003).
- ¹⁰C. Jiang, F. Hasoon, H. Moutinho, H. Al-Thani, M. Romero, and M. Al-Jassim, *Appl. Phys. Lett.* **82**, 127 (2003).
- ¹¹D. Schmid, M. Ruckh, F. Grunwald, and H. Schock, *J. Appl. Phys.* **73**, 2902 (1993).
- ¹²A. Niemegeers, M. Burgelman, R. Herberholz, U. Rau, D. Hariskos, and H. Schock, *Prog. Photovoltaics* **6**, 407 (1998).
- ¹³M. Igalson, M. Bodegard, and L. Stolt, *Sol. Energy Mater. Sol. Cells* **80**, 195 (2003).
- ¹⁴S. Lany and A. Zunger, *J. Appl. Phys.* **100**, 113725 (2006).
- ¹⁵S. Lany and A. Zunger, *Phys. Rev. Lett.* **100**, 016401 (2008).
- ¹⁶M. Igalson, A. Urbaniak, and M. Edoff, *Thin Solid Films* **517**, 2153 (2009).

- ¹⁷M. Igalson, P. Zabierowski, D. Przado, A. Urbaniak, M. Edoff, and W. Shafarman, *Sol. Energy Mater. Sol. Cells* **93**, 1290 (2009).
- ¹⁸L. Chernyak, K. Gartsman, D. Cahen, and O. Stafsudd, *J. Phys. Chem. Solids* **56**, 1165 (1995).
- ¹⁹R. Herberholz, H. Schock, U. Rau, J. Werner, T. Haalboom, T. God-ecke, F. Ernst, C. Beilharz, K. Benz, and D. Cahen, in *Conference Record of the Twenty Sixth IEEE Photovoltaic Specialists Conference* (1997), p. 323.
- ²⁰Q. Nguyen, K. Orgassa, I. Koetschau, U. Rau, and H. Schock, *Thin Solid Films* **431–432**, 330 (2003).
- ²¹C. A. Kaufmann, R. Caballero, T. Unold, R. Hesse, R. Klenk, S. Schorr, M. Nichterwitz, and H. Schock, *Sol. Energy Mater. Sol. Cells* **93**, 859 (2009).
- ²²A. Gabor, J. Tuttle, M. Bode, A. Franz, A. Tennant, M. Contreras, R. Noufi, D. Jensen, and A. Hermann, *Sol. Energy Mater. Sol. Cells* **41–42**, 247 (1996).
- ²³C. A. Kaufmann, A. Neisser, R. Klenk, and R. Scheer, *Thin Solid Films* **480–481**, 515 (2005).
- ²⁴C. Donolato, *J. Appl. Phys.* **66**, 4524 (1989).
- ²⁵M. Burgelman, P. Nollet, and S. Degraeve, *Thin Solid Films* **361–362**, 527 (2000).
- ²⁶J. Rechid, A. Kampmann, and R. Reinek-Koch, *Thin Solid Films* **361–362**, 198 (2000).
- ²⁷M. Nichterwitz, “Charge carrier transport in Cu(In,Ga)Se₂ thin-film solar-cells studied by electron beam induced current and temperature and illumination dependent current voltage analyses,” Ph.D. dissertation (Technische Universität, Berlin, 2012).
- ²⁸W. Shockley and W. Read, *Phys. Rev.* **87**, 835 (1952).
- ²⁹T. Eisenbarth, T. Unold, R. Caballero, C. A. Kaufmann, and H. Schock, *J. Appl. Phys.* **107**, 034509 (2010).
- ³⁰S. Wei and A. Zunger, *J. Appl. Phys.* **78**, 3846 (1995).
- ³¹S. Wei, S. Zhang, and A. Zunger, *Appl. Phys. Lett.* **72**, 3199 (1998).
- ³²P. Migliorato, J. Shay, H. Kasper, and S. Wagner, *J. Appl. Phys.* **46**, 1777 (1975).
- ³³D. Schmid, M. Ruckh, and H. Schock, *Sol. Energy Mater. Sol. Cells* **41–42**, 281 (1996).
- ³⁴M. Ruckh, D. Schmid, M. Kaiser, R. Schaffler, T. Walter, and H. Schock, in *Conference Record of the IEEE Photovoltaic Specialists Conference I and II* (1994), p. 156.
- ³⁵R. Kimura, T. Mouri, T. Nakada, S. Niki, A. Yamada, P. Fons, T. Matsuzawa, K. Takahashi, and A. Kunioka, *Jpn. J. Appl. Phys., Part 2* **38**, L899 (1999).
- ³⁶S. Chaisitsak, A. Yamada, and M. Konagai, *Jpn. J. Appl. Phys., Part 1* **41**, 507 (2002).
- ³⁷M. Gloeckler and J. Sites, *Thin Solid Films* **480**, 241 (2005).